DOT/FAA/AR-01/27

Office of Aviation Research
Washington, D.C. 20591

Engine Debris Fuselage Penetration Testing, Phase I

August 2001

Final Report

This document is available to the U.S. public
through the National Technical Information
Service (NTIS), Springfield, Virginia 22161.

U.S. Department of Transportation
Federal Aviation Administration

20011120 078

NOTICE

1. Report No. DOT/FAA/AR-01/27	2. Government Accession No.	3. Recipient's Catalog No.	
4. Title and Subtitle ENGINE DEBRIS FUSELAGE PENETRATION TESTING, PHASE I		5. Report Date August 2001	
		6. Performing Organization Code NAWCWD 418300D	
7. Author(s) Steven J. Lundin		8. Performing Organization Report No.	
9. Performing Organization Name and Address Commander Naval Air Warfare Center Weapons Division 1 Administration Way China Lake, CA 93555-6001		10. Work Unit No. (TRAIS)	
		11. Contract or Grant No.	
12. Sponsoring Agency Name and Address U.S. Department of Transportation Federal Aviation Administration Office of Aviation Research Washington, DC 20591		13. Type of Report and Period Covered Final Report	
		14. Sponsoring Agency Code ANE-100	
15. Supplementary Notes			

16. Abstract

During February 1999, the Naval Air Warfare Center Weapons Division (NAWCWD), China Lake, conducted a series of simulated uncontained engine failure structural impact tests. A large gas gun was used to launch turbine engine fan blade segments into an aircraft fuselage. The impacts were documented and analyzed with high-speed photography. Impact velocities, presented areas, and residual velocities were calculated. The data were then compared to analytic results predicted by the Joint Technical Coordinating Group for Munitions Effectiveness (JTCG/ME) penetration equations. These equations were originally develop to predict the penetration and residual velocity of ballistic weapon projectiles upon impact with various vehicles. The ballistic prediction equations developed for warhead fragments are the closest in geometric shape to turbine engine blade fragments. The data comparison shows good agreement for the predicted and experimental residual velocities.

17. Key Words Engine debris mitigation testing, Uncontained fuselage penetration		18. Distribution Statement This document is available to the public through the National Technical Information Service (NTIS), Springfield, Virginia 22161.	
19. Security Classif. (of this report) Unclassified	20. Security Classif. (of this page) Unclassified	21. No. of Pages 31	22. Price

Form DOT F1700.7 (8-72) Reproduction of completed page authorized

TABLE OF CONTENTS

Page

LIST OF FIGURES

LIST OF TABLES

iv

EXECUTIVE SUMMARY

This work was conducted under the sponsorship and oversight of the Federal Aviation Administration (FAA) Airport and Aircraft Safety R&D Divisions, Engine and Propeller Directorate and the Transport Airplane Directorate. The Uncontained Engine Debris Mitigation Program (UEDMP) falls under the Catastrophic Failure Prevention Program which is managed by the Airworthiness Assurance R&D Branch of the FAA William J. Hughes Technical Center.

During February 1999, the Naval Air Warfare Center Weapons Division (NAWCWD), China Lake, conducted a series of simulated uncontained engine failure structural impact tests. A large gas gun was used to launch turbine engine fan blade segments into an aircraft fuselage. The impacts were documented and analyzed with high-speed photography. Impact velocities, presented areas, and residual velocities were calculated. The data were then compared to analytic results predicted by the Joint Technical Coordinating Group for Munitions Effectiveness (JTCG/ME) penetration equations. These equations were originally develop to predict the penetration and residual velocity of ballistic weapon projectiles upon impact with various vehicles. The ballistic prediction equations developed for warhead fragments are the closest in geometric shape to turbine engine blade fragments. The data comparison shows good agreement for the predicted and experimental residual velocities.

1. INTRODUCTION.

1.1 PURPOSE.

The objective of this testing is to measure the residual velocities of actual aircraft structure impacts and make refinements to the empirical methodology used to predict debris penetration of aircraft structures. To that end, the equations will be further validated, complex structural areas will be impacted, and actual commercial aircraft components will be used.

1.2 BACKGROUND.

The damaging effects from an uncontained aircraft turbine engine failure can be catastrophic. As a result, the Federal Aviation Administration (FAA) has commissioned a program to mitigate the damaging effects of such an event. The Uncontained Engine Debris Mitigation Program will work with industry and government to determine possible engineering solutions to this problem.

As part of this program, the Naval Air Warfare Center Weapons Division (NAWCWD) has been tasked to evaluate ballistic damage analysis tools and techniques which are currently in use by the defense community. The intent is to determine their applicability in predicting the damaging effects from an uncontained engine failure. This report documents testing which was conducted in the evaluation of these equations.

1.2.1 The JTCG/ME Penetration Equations.

Among the analysis tools currently in use are the Joint Technical Coordinating Group for Munitions Effectiveness (JTCG/ME) penetration equations. These equations were originally developed to predict the penetration and residual velocity of ballistic weapon projectiles upon impact with various materials. Of particular interest are the ballistic prediction equations which were developed for warhead fragments, as these fragments are closest in geometric description to turbine engine blade fragments. The JTCG/ME penetration equations are listed as follows.

The Residual Velocity Equation:

$$V_r = \frac{\sqrt{V^2 - V_{50}^2}}{1.0 + \dfrac{\rho A_p t}{W \cos\theta}} \tag{1}$$

The Ballistic Limit Equation:

$$V_{50} = C_{bf} \left(\frac{\rho_f t A_p}{W} \right)^{b_f} \sec^h \theta \left(\frac{\rho_f t A_p}{W_o} \right)^f \tag{2}$$

1

Where:

V = debris initial velocity

V_{50} = debris ballistic limit velocity. Penetration occurs 50% of the time.

V_r = debris residual velocity

ρ_f = debris specific weight (debris weight/volume)

ρ = plate specific weight (plate weight/volume)

t = plate thickness

A_p = debris presented area along direction of travel

1.2.2 Empirical Constants.

The penetration equations have been incorporated into a computer model as one possible analysis tool for aircraft designers. The Uncontained Debris Model (UDM) focuses on blade fragment debris as this type of debris is most likely to result from an uncontained engine event. According to extensive investigation, this is the most likely particle, which would result in damage to an aircraft. The debris model identifies the debris type by component (fan blade, turbine blade, compressor blade) and defines the most likely size, mass, and velocity for each debris fragment.

1.3 RELATED ACTIVITIES/DOCUMENTS.

In 1998, NAWCWD conducted its first series of impact tests for the FAA. That work is documented in reference 1. The first tests used aircraft cowl sections as targets. The projectiles were small pieces of aluminum (simulated fragment), and medium sized fan, compressor, and turbine blade fragments.

Scientists from SRI International participated in the tests documented here by conducting some experiments with Kevlar and Zylon reinforcements on the interior wall panels of the aircraft. Their work is documented in reference 2.

2. DISCUSSION OF TEST AND TEST RESULTS.

Predicting the survivability of aircraft structures requires an understanding of the vulnerability of various types of structures to impacts from debris caused by uncontained engine failures. The debris produced comes in all shapes and sizes and at speeds that vary from 300 to 800 ft/s. Understanding the nature of the impact may lead to simple and inexpensive techniques to improve aircraft safety. This work examines an empirical residual energy calculation method and correlates realistic impacts to the model.

The model evaluated here calculates residual velocity and V_{50}, given a series of plates of known thickness, impact kinematics, and projectile mass properties. This testing is the first collection of impact data for situations resembling actual aircraft incidents. The existing equations were developed for 50 caliber bullets. Over the past 10 years they have been refined with test data to provide a better description of irregular projectiles resembling warhead fragments and turbine engine debris.

This current testing adds to the aircraft incident reports and provides a higher quality of data due to the high speed photographic documentation. Analysis of an impact requires knowledge of the projectile's orientation with respect to the target, velocity, and the residual velocity. The orientation of the projectiles just prior to impact has been very difficult to estimate. Projectile orientation is critical to estimating the energy exchange at impact. High-speed motion picture cameras provide images that can be used to measure the orientation of the projectile.

During just over 1 month of testing a total of 66 shots were attempted. Of these, 45 were fully successful and 6 were partially successful. The partially successful shots were those that did not penetrate the skin. The balance of the shots were not useable for penetration calculations due to test anomalies such as, blade not separating from the sabot (gas gun projectile carrier), sabot failure in the muzzle, high-speed film camera malfunction, and light malfunctions. On the occasions where the sabot failed in the muzzle, the blade would impact the sabot stopper and then not impact the fuselage in the region of film coverage. In cooperation with SRI International, 16 test shots were conducted that involved skin and interior wall panels (IWP) with and without energy absorbing material. This work was documented in reference 2.

2.1 PRESENTED AREA MEASUREMENT METHODOLOGY.

The best method for determining presented area at impact is the have two high-speed film views of the fragment in flight. For any point in three-dimensional (3D) space, knowing the projected coordinates for any two planes fully describes the 3D point. Therefore, two cameras set up along orthogonal axes will easily produce corner data from an image that can be transformed into body attitudes. Early in the testing, problems were encountered with locating the two external cameras at right angles. It became clear the side camera would work, but the up or down camera would often not be locatable such that the two views would be orthogonal. The aircraft structure and other rigging became obstructions.

Since two views of the fragment in flight was not possible, a methodology needed to be developed that would calculate the presented area from one view. Two observations provided the insight into the solution. First, blade fragments usually had very little angular momentum when exiting the sabot stopper. Second, the impact hole geometry provided an indication as to the general orientation of the blade. Projectile corner x,y data from the side view was input to an Excel spreadsheet model. The model contained a geometric description of the blade based on measurements taken before the shot. After appropriate transformations, the model blade was rotated about three axes until a best fit to the high-speed film data was obtained. The blade model was of a cambered plate of no thickness. The thickness was input to the model as camber. The process was automated by using the Excel Solver. The Solver tool was allowed to vary all three rotation angles. The optimizer's goal was to minimize the sum of the root sum squared errors between the model blade and the film data corner locations.

The procedure was scrutinized for every shot. Because the physical situation was fairly well understood, it was possible to quickly spot situations where the method had failed to find the applicable solution. When the solution was incorrect, typically, the roll angle would have the wrong sign. Using the launch attitude as a first guess for the optimizer usually produced the best fit. Reference frames for this analysis are shown in figures 1 through 4.

3

BLADE FRAGMENT

X_I
Z_I
Y_I

SABOT STOPPER PLATE

X_B
V
Z_B
Y_B
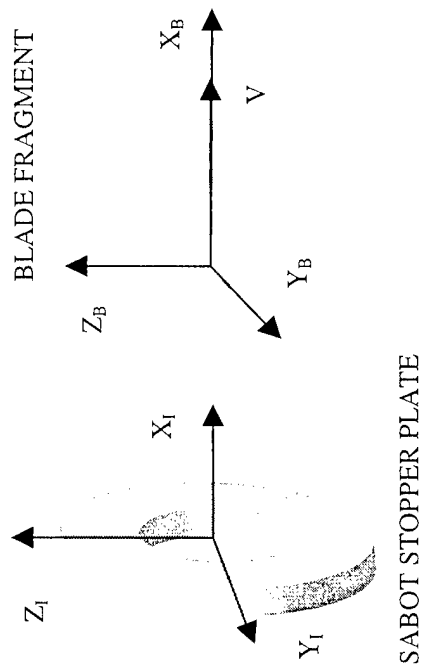
FIGURE 1. LEFT HAND REFERENCE FRAME

BLADE FRAGMENT

X_I
Z_I
Y_I

SABOT STOPPER PLATE

+YAW, ψ
$X_{B'}$
V
$Z_{B'}$
$Y_{B'}$
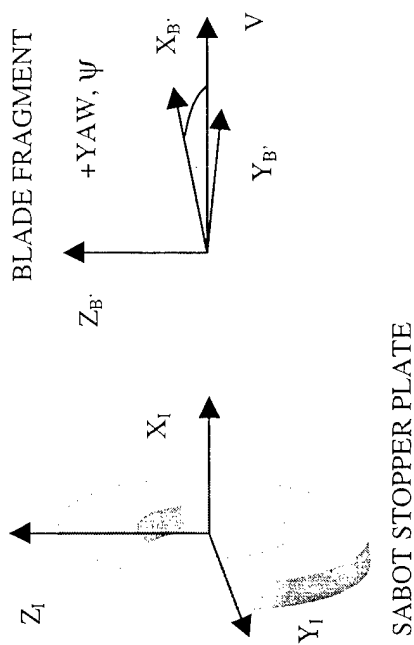
FIGURE 2. FRAGMENT YAW DEFINITION

BLADE FRAGMENT

+PITCH, θ
$X_{B''}$
$X_{B'}$
X_I
Z_I
Y_I
$Z_{B''}$
V
$Y_{B''}$

SABOT STOPPER PLATE
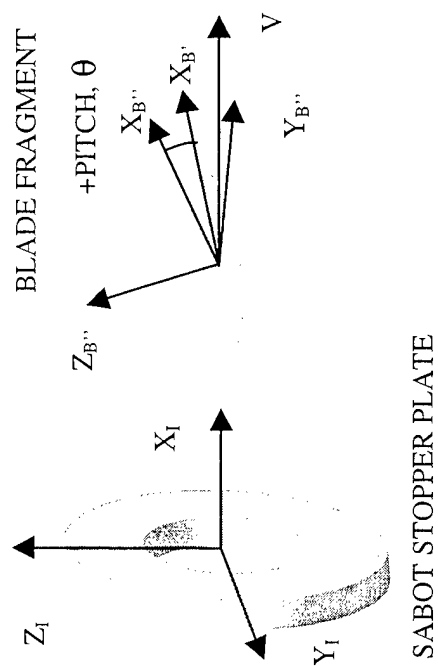
FIGURE 3. FRAGMENT PITCH DEFINITION

BLADE FRAGMENT

X_I
Z_I
Y_I
$X_{B''}$
V
$Y_{B''}$
$Y_{B'''}$
$Z_{B''}$
+ROLL, ϕ

SABOT STOPPER PLATE
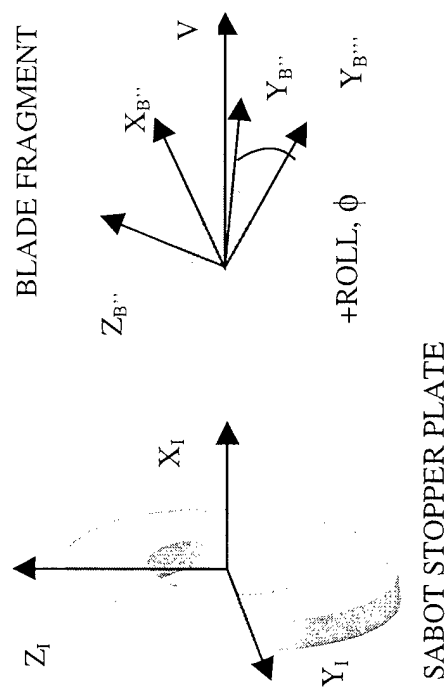
FIGURE 4. FRAGMENT ROLL DEFINITION

4

2.2 TEST SETUP.

An aircraft fuselage center section approximately 40 ft. long was used as the target for these test shots. The projectiles were cut from fan blades. There were two size categories, 3 by 8 in. and 3 by 5 in. with weights in the 0.75 and 0.4 lb. ranges respectively. These fragments were fired from a nitrogen gas gun at speeds from 300 to 800 ft/s. The projectiles were launched with a sabot that imparted very small angular momentum to the fragments. This provided for highly accurate aim and good control of orientation at impact.

The test setup is shown in figure 5. The fuselage could be rolled ±30 degrees and translated along a track to line up the different target areas. The gun had a limited elevation control and was typically close to horizontal and aligned with the upper radius of the fuselage section. Table 1 displays the fragment launch orientations and the shotline obliquities for each of the test shots. The fragment pitch angle was limited by the diameter of the gun and the sabot design. It was determined that with initial pitch angles of 15° the polystyrene foam in the sabot would fail randomly and result in spectacular fragment and sabot stopper plate impacts. For this reason most of the shots were at a reliable 0 degrees pitch.

Figures 6 and 7 show examples of the fan blade fragments used in these tests. They were cut from a used fan blade. The reflective tape was used to enhance the blade visibility in the high-speed film. Typically, after a test a blade was reusable. The corners would get chipped away but the fragments seldom broke up. The large blades were 7 to 9 in. long and about 3 by 0.25 inch thick. The medium size blades were about half the length of the large ones. SRI International shot some 25-gram 1.3 by 1.0 by 0.25 inch projectiles.

FIGURE 5. TEST SETUP SHOWING GAS GUN AND FUSELAGE

5

TABLE 1. FRAGMENT ORIENTATIONS AND OBLIQUITIES

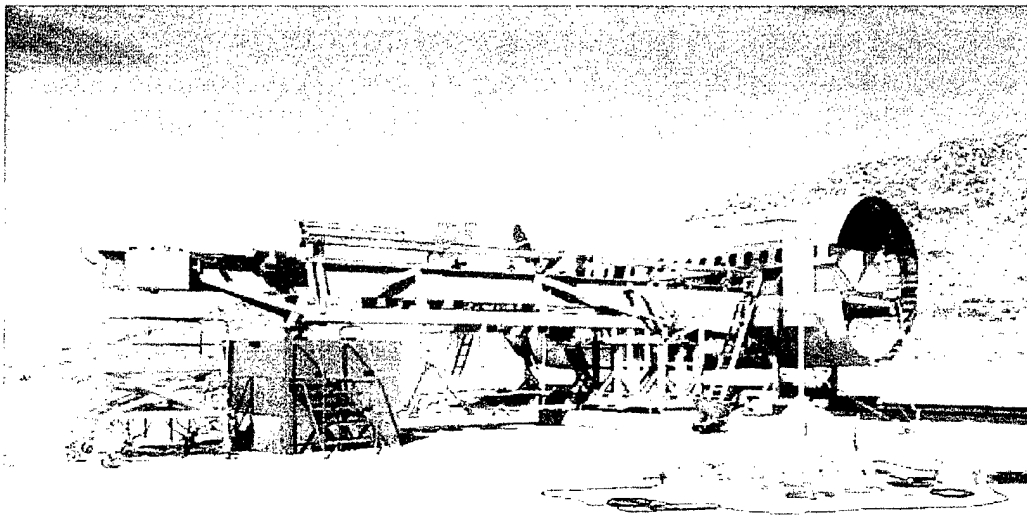| Shot No.	Shot Category	Blade Type	Pitch (deg)	Roll (deg)	Obliquity (deg)
1	skin	Large	0	45	3
2	skin	Large	0	0	3
3	skin	Large	10	0	3
4	skin + Z-stringer	Large	0	30	7
5	skin	Large	15	90	7
6	skin	Large	0	-45	3
7	skin + Z-stringer	Large	0	90	8
8	skin + Z-stringer	Large	0	90	8
9	skin + Z-stringer	Medium	0	45	8
10	skin + Hat-stringer	Medium	0	120	8
11	skin + Hat-stringer	Medium	0	0	8
12	skin	Medium	0	0	8
13	skin + rib	Large	0	0	8
14	skin + rib	Large	10	180	8
15	skin + rib	Large	20	180	8
16	skin	Large	10	-90	8
17	skin	Large	20	90	8
17.5	skin	Medium	0	90	8
19	skin	Medium	0	45	10
20	skin	Large	0	45	10
21	skin + rib	Large	10	90	14
22	skin + Hat-stringer	Large	0	90	14
23	skin	Large	0	90	8
24	skin	Large	0	0	8
25	skin	Large	20	0	8
26	skin + Hat-stringer	Large	20	90	8
26.5	skin + Hat-stringer	Large	10	90	8
27	skin + Hat-stringer	Large	10	0	8
28	skin + rib	Large	20	90	8
28.5	skin + rib	Large	10	180	8
29	skin + rib	Large	20	180	8
30	skin + rib	Large	0	0	8
31	skin + rib	Large	0	0	8
32	skin + rib	Large	15	0	8
33	skin + rib	Large	10	90	8
34	skin + rib	Large	10	45	8
35	skin	Large	15	90	8
36	skin + Z-stringer	Large	15	0	8
37	skin	Large	0	45	8
38	skin + IWP	Small	0	90	3
39	skin + IWP	Small	0	90	3
40	skin + IWP	Small	0	90	3
41	skin + IWP	Medium	15	90	8
42	skin + IWP	Small	0	90	3
43	skin + IWP	Small	0	90	3
44	skin + IWP	Small	0	90	3
45	skin + IWP	Small	0	90	3
46	skin + IWP	Medium	0	45	3
47	skin + IWP	Medium	0	135	3
48	skin + IWP	Medium	0	45	3
49	skin + IWP	Medium	0	45	3
50	skin + IWP	Medium	0	45	3
51	skin + IWP	Medium	0	45	3
52	skin + IWP	Medium	0	45	3
53	skin + IWP	Medium	0	60	3
54	skin + fuel tubing	Large	0	0	8
55	skin + fuel tubing	Large	0	0	8
56	skin + fuel tubing	Large	0	0	8
57	skin	Large	0	0	8
58	skin	Large	0	0	8
59	skin	Large	0	0	8
60	complex w/cables	Medium	10	0	
61	complex w/cables	Large	0	0	
62	complex w/cables	Large	0	90	
63	complex w/cables	Large	0	90	
64	complex w/cables	Large	0	45	

6
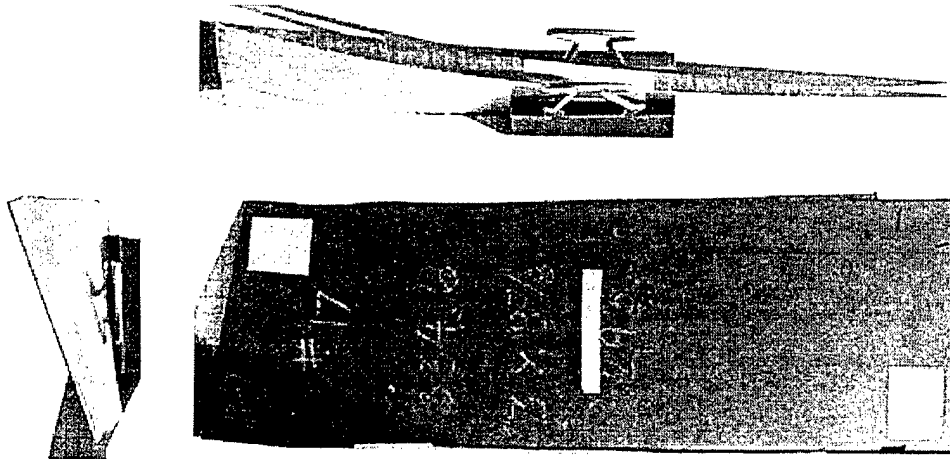
FIGURE 6. LARGE BLADE FRAGMENT USED IN SHOT 26B
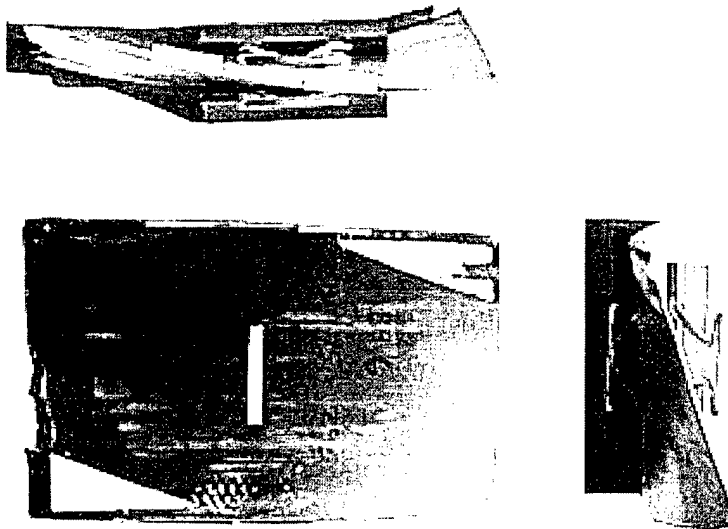
FIGURE 7. MEDIUM BLADE FRAGMENT USED IN SHOT 41

An example of the sabots can be seen in figure 8. A coffee can, Teflon, and Styrofoam to build the sabots were used. The Teflon was used as a backing plate to prevent the gas blast from destroying the foam. The coffee can had to be made slightly smaller in diameter to fit the gun, but worked wonderfully. The previous tests' sabot designs were very heavy and outweighed the projectile by many times. Stopping those sabots at the energies of this test was going to be expensive. Three sabot stopper plates of 3 in. Society of Automotive Engineers (SAE) 4140 steel were broken during the pretest experiments.

It should be noted that roll angles are approximate due to the muzzle loading nature of the gun. The sabot/fragment unit usually is loaded straight down the muzzle but on occasion it rotated slightly. The table values are estimated to be within 5 deg. of actual angles. The obliquity angles could not be selected for each shot. They were dictated by the shot location.

FIGURE 8. FINAL SABOT DESIGN WITH LOADED FRAGMENT

Two high-speed motion picture cameras were used outside to provide a side view and an up view of the impact. The up-view was problematic due to the aircraft structure sometimes blocking the view. Large remote controlled mirrors were used to reflect sunlight onto the shotline. Backboards were setup with 12 in. grids that provided the calibration for measurements. The cameras were set to run at 6000 pictures per second with shutter speeds of 1/15,000 second. The film used was Kodak Estar Base Ektachrome type 2239 in 250 ft. lengths on daylight rolls.

The interior, as shown in figure 9, displays the backboard and particleboard projectile catcher. The interior wall panels, trim, overhead stowage, and insulation were removed. Two, 2000 Watt cinema lights were used to illuminate the scene.
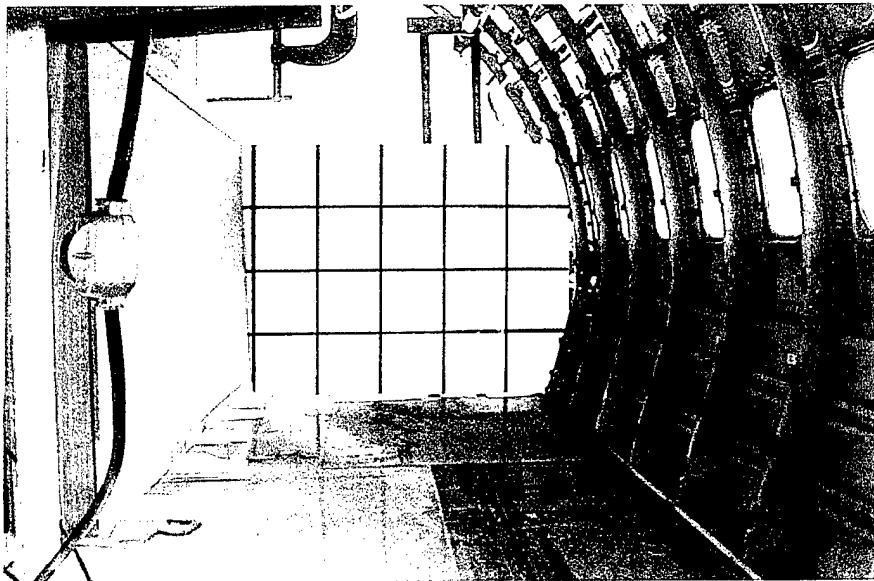
FIGURE 9. INTERIOR SETUP OF AIRCRAFT FUSELAGE

8

2.3 TEST PROCEDURE.

The test procedure used for each shot is outlined below.

1. The fuselage section was rolled and translated to bring the desired target location into the center of the view down the gas gun barrel.

2. The backstop position in the fuselage was checked and relocated as necessary to provide for fragment capture.

3. The high-speed film cameras' control lines were checked.

4. The lights' control lines were checked.

5. The gas gun control lines were checked.

6. The camera to grid board and camera to shotline measurements were made for all cameras.

7. The blade fragment was measured and weighed.

8. The blade fragment was digitally photographed and placed in the sabot.

9. The high-speed film cameras were loaded and armed.

10. The sabot with fragment was muzzle loaded and pushed 10 ft. down the muzzle.

11. The test area was cleared of personnel.

12. The gas gun was charged with nitrogen to a pressure required for the shot velocity.

13. The electronic test sequencer was started and a t-15 second count was begun.

14. Digital images were made of the entrance and exit sides of the hole.

15. The hole was marked for identification.

16. The high-speed cameras were unloaded.

17. The shot area was cleaned up.

A map of the shot locations for the cabin area test is shown in figure 10. Each shot number and it's location on the fuselage are shown in the figure. The windows are numbered from aft forward. The complex structure shots, test 60-64 are shown in figure 11.

During the testing, it became evident that the skin thickness varied greatly across some of the shot locations. The thickness is an important factor, therefore two or three measurements were made and averaged after each shot. This map of thickness is presented in figure 12. The units are inches and the bold numbers are starboard side measurements assumed to be similar to the port side. The crosshatched areas are where the fuselage had been repaired and were undesirable for testing. The drawing is not drawn to scale but for planning purposes only. It depicts the general arrangement of the ribs, windows, and stringers.

9
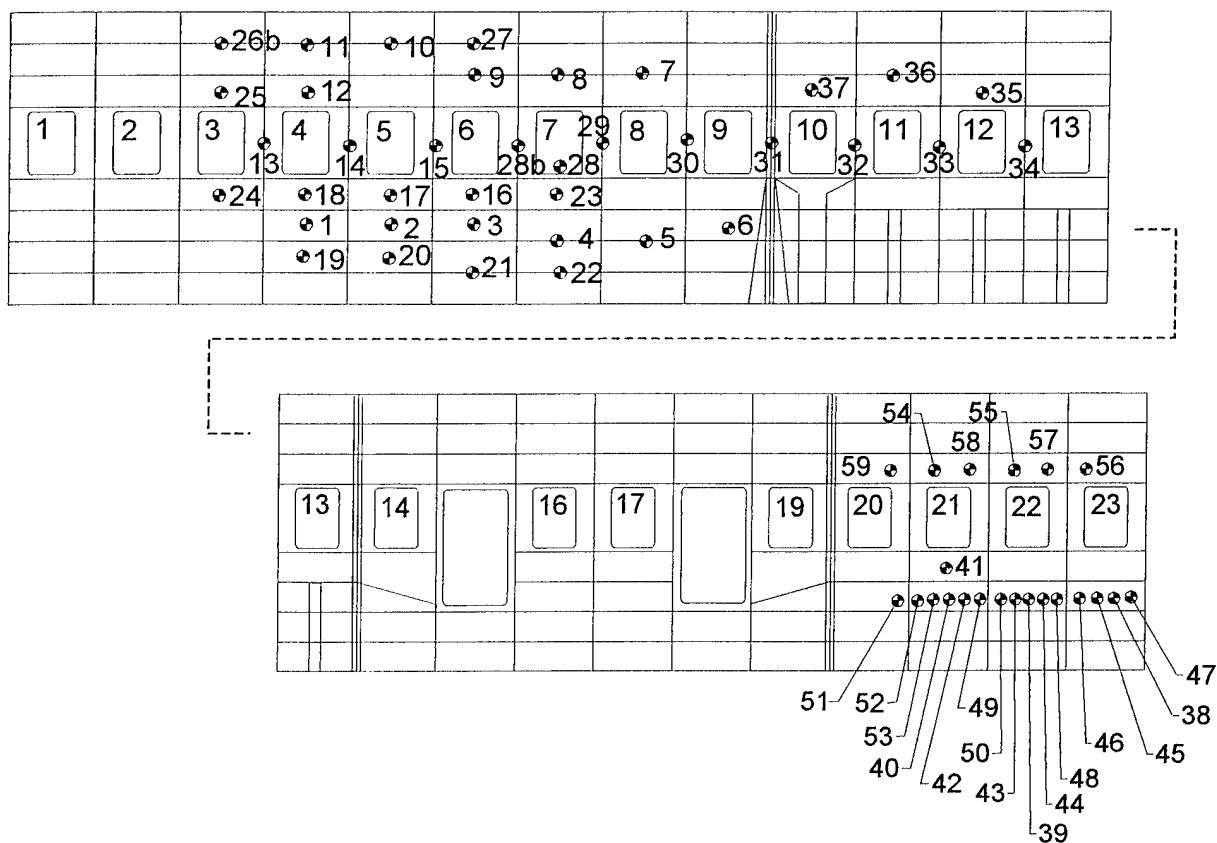
FIGURE 10. AIRCRAFT FUSELAGE SHOT MAP, INTERIOR VIEW
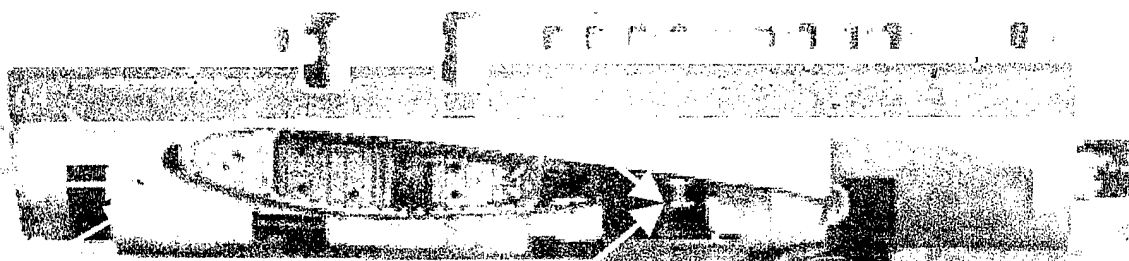
FIGURE 11. AIRCRAFT FUSELAGE TESTS 60-64 LOCATIONS

FIGURE 12 — Thickness map tables (values in inches):

Top map:

	0.065	0.060	0.070 0.060	0.063	0.071 0.066		0.073		0.078		0.084	
								0.086				
0.083	0.083	0.097	0.085				0.188	0.197	0.142	0.184	0.266	
1 0.105	2 0.108	3 0.094	4 0.101	5 0.132	6 0.134	7	8 0.144	9	10 0.180	11	12	13
0.082		0.084	0.084	0.088			0.109	0.247		0.142	0.145	0.268
0.068	0.095	0.071	0.090	0.0063			0.114 0.114	0.142				
0.069	0.065	0.068	0.068	0.062		0.100						

Bottom map:

	0.082		0.082	0.078		0.100		0.060	
0.266						0.137	0.083	0.065	0.047
13	14		16	17	19	20	21	22	23
0.268			0.210	0.210		0.207	0.159		0.054
			0.111	0.112		0.095	0.083	0.075	0.066

FIGURE 12. THICKNESS MAP OF THE PORTSIDE CABIN TEST AREA (inches)

2.4 TEST RESULTS.

2.4.1 Analysis Discussion.

The UDM penetration equations are capable of modeling multiple layers of plates but not a stringer or rib. With this body of experimental data an analysis was done to determine if the equations could be useful for impacts that involved stringers and ribs. This analysis used a simple approach. For the initial investigation, the rib or skin would be modeled as a second plate of the thickness of the rib or stringer.

Table 2 shows the input parameters to the penetration equations. The penetration equations compute the presented area, residual velocity, (V$_{50}$) and residual energy for the impact. In reducing this data, the presented area for each impact was computed.

TABLE 2. PENETRATION EQUATIONS INPUT PARAMETERS

Fragment width
Fragment height
Fragment weight
Release velocity
Obliquity angle
Number of plates
Plate thickness for each plate
Fragment angle for each plate
Material type for each plate

11

For these tests, all of the parameters could be measured directly except for the fragment impact angle. The penetration equations do not have a 3-D model of the impact. The presented area was used to obtain the correct fragment angle. For each shot, a fragment angle was chosen that produced the presented area obtained from the high-speed film analysis.

2.4.2 Results.

Figures 13 through 17 show the results of the residual velocity comparisons for each of the structural combinations tested. In the figures, Vi is the impact velocity, Res V is the residual velocity from the high-speed film data, and Vr UDM is the residual velocity predicted with the penetration equations. Table 3 summarizes the shot results using the high-speed camera data. Table 4 summarizes the penetration equation results.
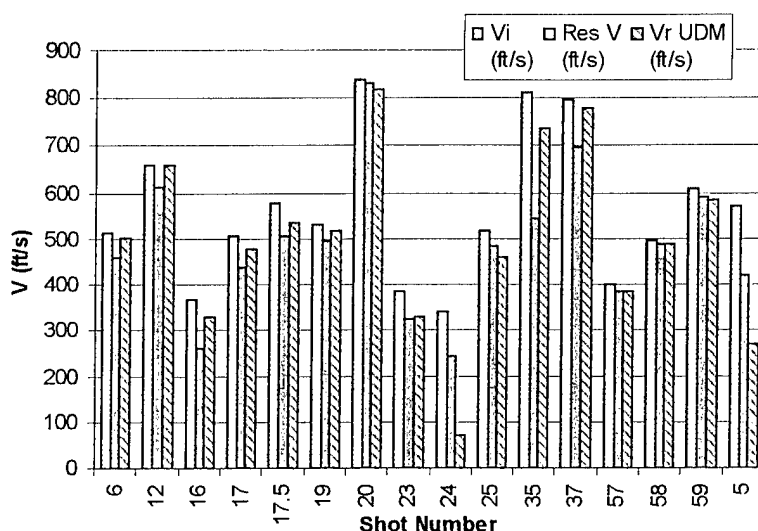
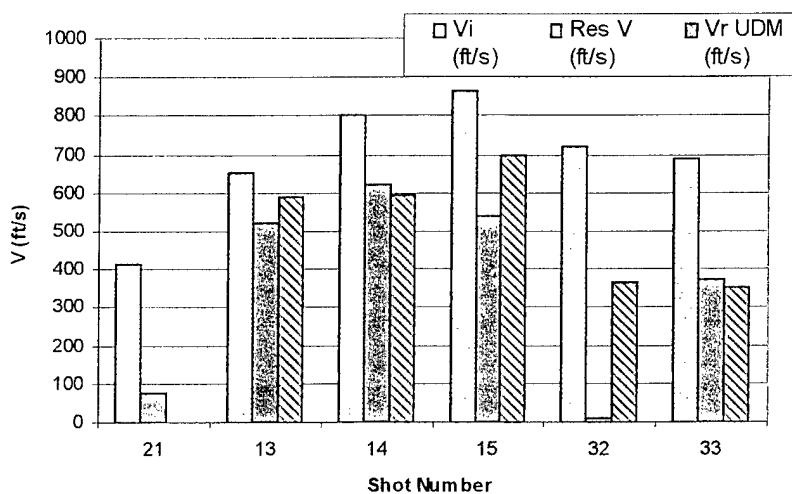FIGURE 13. VELOCITY COMPARISON FOR IMPACTS INVOLVING SKIN ONLY

FIGURE 14. VELOCITY COMPARISON FOR IMPACTS INVOLVING
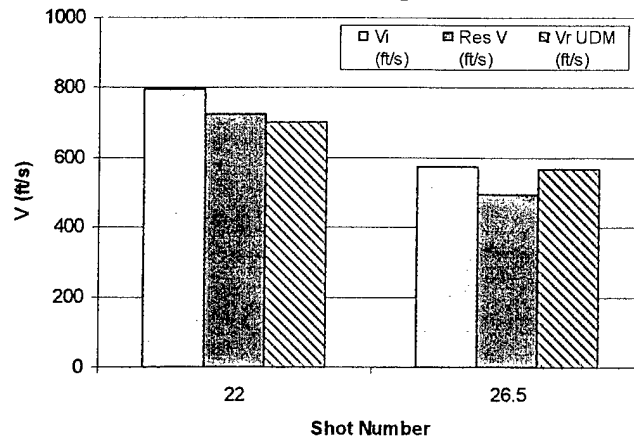SKIN RIB ELEMENTS

12

FIGURE 15. VELOCITY COMPARISON FOR IMPACTS INVOLVING
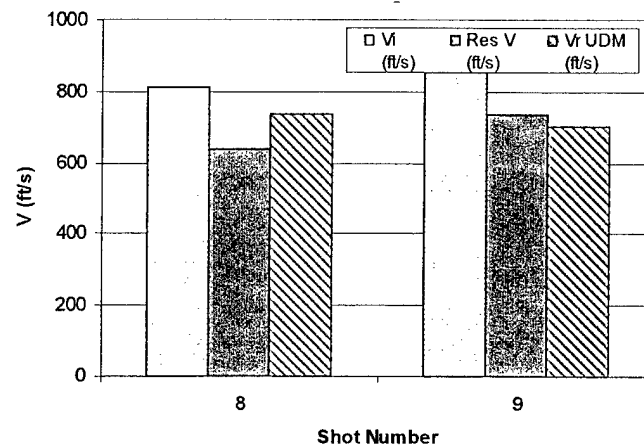SKIN AND HAT-STRINGER ELEMENTS

FIGURE 16. VELOCITY COMPARISON FOR IMPACTS INVOLVING
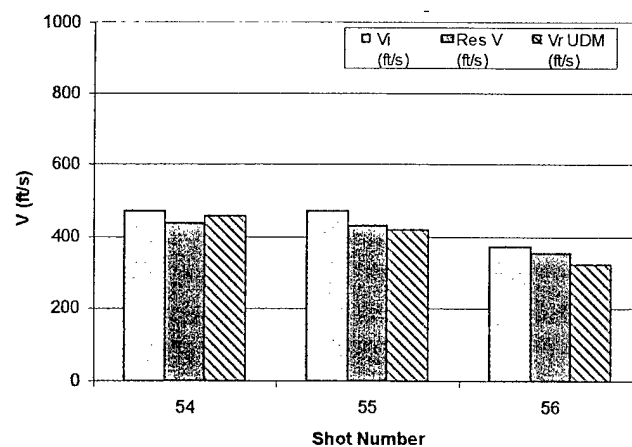SKIN AND Z-STRINGER ELEMENTS

FIGURE 17. VELOCITY COMPARISON FOR IMPACTS INVOLVING
SKIN AND FUEL TUBING

13

TABLE 3. HIGH-SPEED FILM ANALYSIS RESULTS

Shot No.	Shot Category	Wt p (gm)	Vel (ft/s)	Res V (ft/s)	A_p (sq in)	Length of A_p (in)	Yaw (deg)	Pitch (deg)	Roll (deg)	Obliquity (deg)
1	skin	355.3	437							3
2	skin	340.5	431	417						3
3	skin	310.9	317	0						3
4	skin + Z-stringer	343.7	383	359	5.1	9.5	-11.0	3.7	-36.7	7
5	skin	299.1	572	421	9.7	12.5	-25.1	-3.1	2.3	7
6	skin	333.5	515	462	0.8	6.6	-0.1	1.7	63.6	3
7	skin + Z-stringer	331.9	678	122						8
8	skin + Z-stringer	295.8	813	641	1.4	6.9	0.0	0.0	-90.0	8
9	skin + Z-stringer	180.9	892	735	1.7	7.2	2.3	-0.1	-41.7	8
10	skin + Hat-stringer	184.7	755	751						8
11	skin + Hat-stringer	177.9	931	701	0.9	6.7	4.0	0.0	-25.4	8
12	skin	127.2	658	613	0.5	5.9	0.0	0.3	0.0	8
13	skin + rib	319	655	522	2.7	7.8	1.4	6.7	80.4	8
14	skin + rib	314.8	802	620	5.7	9.8	-0.5	12.7	86.4	8
15	skin + rib	306	867	541	4.6	9.1	-3.7	11.5	-84.0	8
16	skin	335.2	367	263	2.1	9.3	-9.4	-8.2	-33.0	8
17	skin	366	505	441	2.5	7.7	1.3	5.8	56.5	8
17.5	skin	184.6	577	505	1.7	7.1	0.0	0.9	0.0	8
19	skin	144.9	530	497	0.6	7.0	2.5	-0.3	59.3	10
20	skin	328.2	840	833	2.5	8.0	1.3	6.3	48.0	10
21	skin + rib	306.8	416	75	21.5	20.4	75.4	-1.5	6.4	14
22	skin + Hat-stringer	302.5	795	725	1.2	6.7	0.0	-0.8	0.0	14
23	skin	327.5	385	327	3.0	8.0	-6.1	0.0	11.0	8
24	skin	335.2	340	243	7.6	12.2	-10.6	21.3	79.8	8
25	skin	398.1	519	484	4.3	9.2	-1.8	11.0	-54.7	8
26	skin + Hat-stringer	335.2	0							8
26.5	skin + Hat-stringer	334.6	574	494	1.2	8.1	0.0	6.4	0.0	8
27	skin + Hat-stringer	306.3	592	355						8
28	skin + rib	373.2	0							8
28.5	skin + rib	303.5	0							8
29	skin + rib	307.5	0							8
30	skin + rib	309.2	749							8
31	skin + rib	417	838	0	1.4	6.9				8
32	skin + rib	313.6	720	1	4.1	9.1				8
33	skin + rib	327.8	687	373	4.3	8.8	8.3	2.3	18.4	8
34	skin + rib	305	718	0	1.7	7.4	-4.3	-0.1	-35.9	8
35	skin	327.5	811	544	2.7	7.5	0.0	-0.3	0.0	8
36	skin + Z-stringer	299.1	777	0						8
37	skin	340.5	799	698	0.8	6.7	-1.9	0.3	20.2	8
38	skin + IWP	24.9	615	400	0.4	2.1	0.0	-30.2	0.1	3
39	skin + IWP	24.9	631	0	0.4	3.0	14.5	-12.7	-7.9	3
40	skin + IWP	24.9	615	259	0.4	1.9	-41.4	15.4	24.9	3
41	skin + IWP	184.6	595	0	5.3	9.5	16.0	14.8	42.2	8
42	skin + IWP	24.9	0	616						3
43	skin + IWP	24.9	812	0	0.3	2.5	0.0	0.0	-10.1	3
44	skin + IWP	24.9	614	276	0.3	2.5	0.0	0.0	-10.1	3
45	skin + IWP	24.9	601	0	0.7	3.4	30.6	-6.6	11.9	3
46	skin + IWP	152.1	647	592	1.1	6.5	-2.3	3.4	-47.2	3
47	skin + IWP	166	634	419	0.7	6.7	-1.9	0.8	61.1	3
48	skin + IWP	157.7	634	UNK	1.1	6.7	5.4	-5.3	-50.5	3
49	skin + IWP	152.3	520	214	0.7	7.0	2.4	-3.0	59.6	3
50	skin + IWP	166	622	0	0.7	6.7	-4.0	0.3	32.8	3
51	skin + IWP	157.7	619	0	0.7	6.9	3.0	-2.0	49.2	3
52	skin + IWP	166	756	0	0.8	6.6	-1.6	1.0	-70.5	3
53	skin + IWP	157.7	804	0	0.7	6.4	0.0	0.0	-1.0	3
54	skin + fuel tubing	317.3	470	437	1.0	6.5	0.0	0.0	90.0	8
55	skin + fuel tubing	317.3	472	430	1.7	7.2	0.0	0.0	90.0	8
56	skin + fuel tubing	328	373	352	1.6	7.1	2.0	-0.7	-73.2	8
57	skin	343.7	399	386	2.0	8.1	5.9	-2.0	-69.0	8
58	skin	343.7	495	490	0.7	7.5	3.5	2.5	-65.0	8
59	skin	328.2	608	590	1.3	6.8	0.0	0.0	-90.0	8
60	complex w/cables	152.3	0							
61	complex w/cables	310.9	0							
62	complex w/cables	309.1	0							
63	complex w/cables	306.3	0							
64	complex w/cables	333.5	0							

14

TABLE 4. PENETRATION EQUATION RESULTS

Shot No.	Shot Category	Skin thk 1 (in)	Skin thk 2 (in)	Avg Thk (in)	Other Thk (in)	Frag Ang (deg)	PenEqn Vr (ft/s)	PenEqn V_{50} (ft/s)	Ap (sq in)
1	skin	0.061	0.061	0.061					
2	skin	0.068	0.057	0.0625					
3	skin			0					
4	skin + Z-stringer	0.095	0.095	0.095	0.067	79			5.08
5	skin	0.114	0.114	0.114	0.075	75.3	427	333.4	5.81
6	skin	0.146	0.137	0.1415		88.3	502	72.3	0.84
7	skin + Z-stringer	0.184	0.125	0.1545					
8	skin + Z-stringer	0.184	0.184	0.184	0.125	86.5	641	115	1.4
9	skin + Z-stringer	0.184	0.184	0.184	0.125	83	735	144	1.72
10	skin + Hat-stringer	0.063	0.063	0.063	0.032				
11	skin + Hat-stringer	0.057	0.063	0.06	0.034	86.5	864	174.7	0.87
12	skin	0.085	0.084	0.0845		87.7	658	74.3	0.53
13	skin + rib	0.096	0.091	0.0935	0.075	83	522	262.5	2.65
14	skin + rib	0.102	0.1	0.101	0.075	77.4	620	193.5	5.73
15	skin + rib	0.128	0.114	0.121	0.065	78.4	541	440	4.49
16	skin	0.133	0.094	0.1135		85	330	135.7	2.1
17	skin	0.078	0.097	0.0875		83.4	479	115.4	2.52
17.5	skin	0.107	0.08	0.0935		83.4	534	160.3	1.65
19	skin	0.067	0.069	0.068		87.4	519	64.6	0.644
20	skin	0.06	0.063	0.0615		84.1	817	93.3	2.48
21	skin + rib	0.085	0.085	0.085	0.082	18		919	21.22
22	skin + Hat-stringer	0.101	0.099	0.1	0.068	87.1	725	178.7	1.15
23	skin	0.102	0.105	0.1035		82.2	329	175.3	2.95
24	skin	0.089	0.079	0.084		71.5	72	330.8	7.62
25	skin	0.085	0.109	0.097		80	460	191.2	4.3
26	skin + Hat-stringer			0					
26.5	skin + Hat-stringer	0.061	0.058	0.0595	0.036	87.5	494	221.7	1.16
27	skin + Hat-stringer	0.065	0.066	0.0655	0.032				
28	skin + rib			0					
28.5	skin + rib	0.112	0.155	0.1335					
29	skin + rib			0					
30	skin + rib	0.146	0.142	0.144					
31	skin + rib			0		86.7			
32	skin + rib	0.205	0.22	0.2125	0.15	79.3	10	509	4.07
33	skin + rib	0.2	0.2	0.2	0.15	81.4	373	256.3	4.26
34	skin + rib			0					
35	skin	0.23	0.137	0.1835		84.2	737	225.2	2.26
36	skin + Z-stringer			0					
37	skin	0.155	0.238	0.1965		88.4	779	86.1	0.74
38	skin + IWP	0.066	0.066	0.066					
39	skin + IWP	0.064	0.063	0.0635					
40	skin + IWP	0.083	0.083	0.083					
41	skin + IWP	0.156	0.161	0.1585					
42	skin + IWP	0.08	0.075	0.0775					
43	skin + IWP	0.063	0.064	0.0635					
44	skin + IWP	0.063	0.059	0.061					
45	skin + IWP	0.063	0.065	0.064					
46	skin + IWP	0.065	0.07	0.0675					
47	skin + IWP	0.066	0.066	0.066					
48	skin + IWP	0.064	0.06	0.062					
49	skin + IWP	0.068	0.073	0.0705					
50	skin + IWP	0.065	0.07	0.0675					
51	skin + IWP	0.095	0.095	0.095					
52	skin + IWP	0.089	0.095	0.092					
53	skin + IWP	0.083	0.083	0.083					
54	skin + fuel tubing	0.085	0.087	0.086		87.3	437	106	1.05
55	skin + fuel tubing	0.068	0.071	0.0695		85.6	430	119.2	1.71
56	skin + fuel tubing	0.053	0.055	0.054		86.3	352	67.3	1.55
57	skin	0.058	0.062	0.06		85.7	386	71.2	2
58	skin	0.075	0.083	0.079		88.4	490	37.4	0.74
59	skin	0.137	0.136	0.1365		87	585	103.1	1.26
60	complex w/cables								
61	complex w/cables								
62	complex w/cables								
63	complex w/cables								
64	complex w/cables								

Note: Gaps in the data are due to various experimental difficulties; camera or light malfunctions and sabot failures are examples of the sort of things that go wrong.

15

Figure 18 through figure 22 show the normalized residual velocities (1-(Vract-VrUDM)/Vi). A value of 1.0 indicates exact agreement between the penetration equations and the high-speed film data. These plots indicate a good agreement between the UDM methodology and the experimental results.
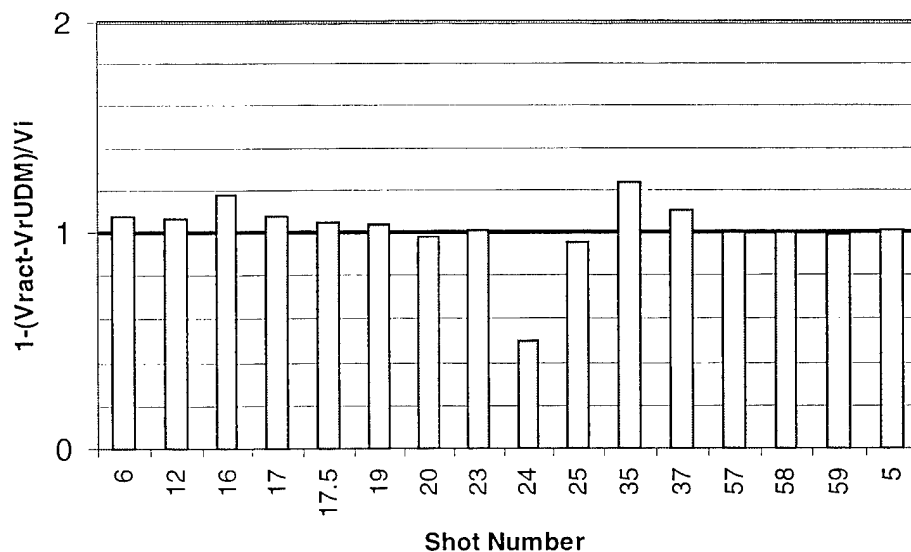

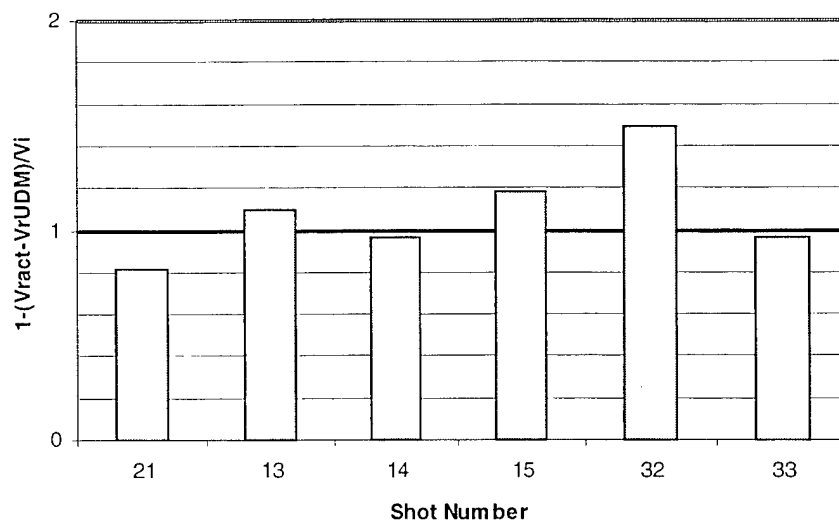FIGURE 18. SKIN ONLY NORMALIZED RESIDUAL VELOCITY COMPARISON

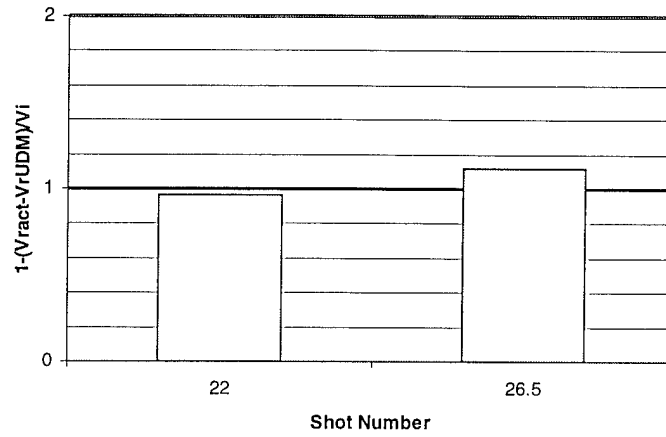FIGURE 19. SKIN AND RIB NORMALIZED RESIDUAL VELOCITY COMPARISON

16

FIGURE 20. SKIN AND HAT STRINGER NORMALIZED RESIDUAL
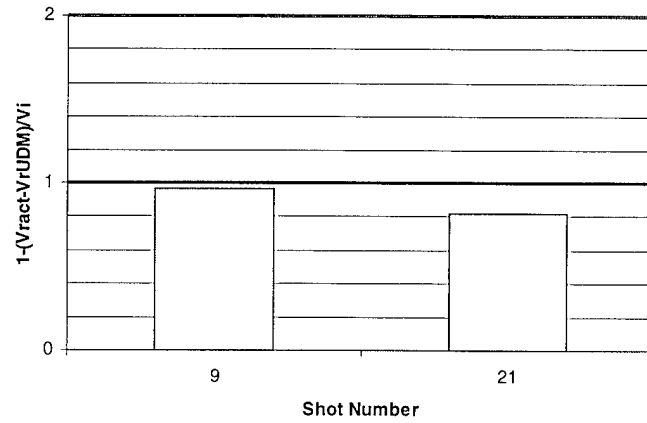VELOCITY COMPARISON

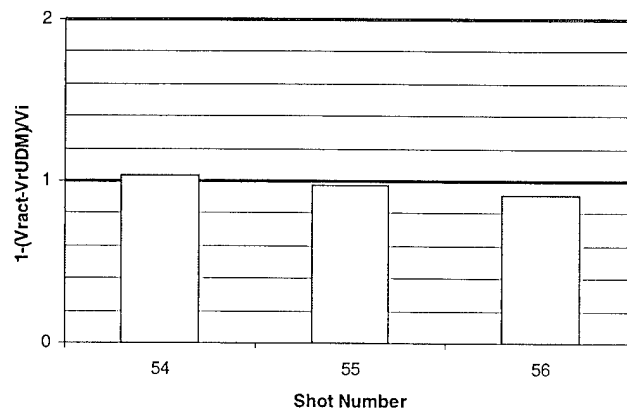FIGURE 21. SKIN AND Z-STRINGER NORMALIZED RESIDUAL
VELOCITY COMPARISON

FIGURE 22. SKIN AND FUEL TUBING NORMALIZED RESIDUAL
VELOCITY COMPARISON

17

The above plots are presented for comparison to the previous test results documented in reference 1. Another way of looking at the problem is to ask how often do specific test cases agree when examining simple skin shots and more complex shots. This analysis shows a less favorable view of the methodology. Table 5 shows the relative agreements of the impact and residual velocities for three categories of shots. The skin and fuel tubing shots are presented as an indication that a modified methodology may be found that produces better agreements.

TABLE 5. PERCENT AGREEMENT BETWEEN ACTUAL AND
PREDICTED RESIDUAL VELOCITY

Structure	Agree Within 5%	Agree Within 10%	Agree Within 20%
Skin Only	43.8	68.8	75.0
Skin and Fuel Tubing	66.0	100.0	100.0
Skin and Any Other	5.0	7.0	10.0

Appendix A contains the documentation of the shots that were conducted as information only. A few shots were made that involved control cable pulleys, control cables, cabin floor, along with ribs, beams, and other structures. They were performed even though the shot geometry precluded the use of high-speed cameras. The information describes the shotline, impact energy, and associated damage. Residual velocities and presented areas are not a product for those shots. This data may be useful in incident investigations where little to no controlled information exists.

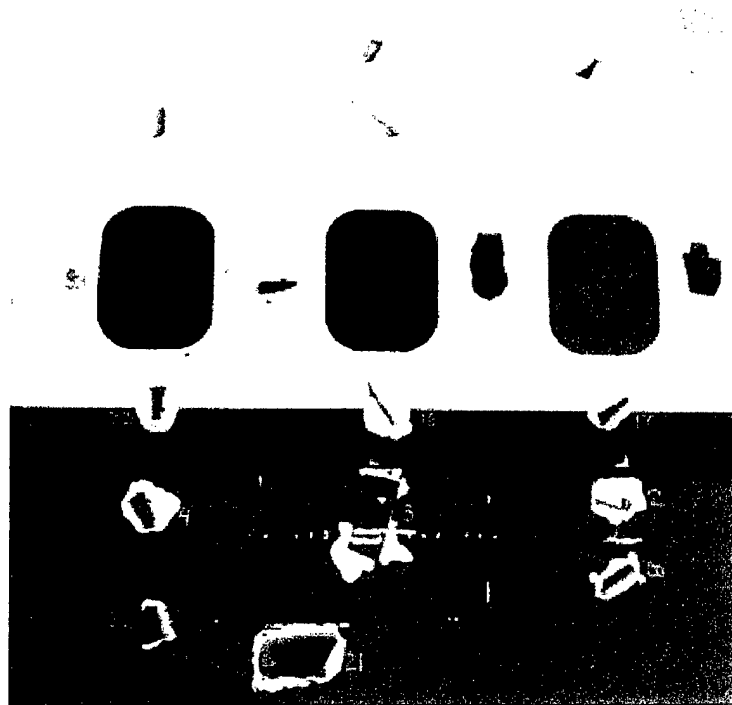Figures 23 and 24 show typical posttest impact areas from the inside and outside.

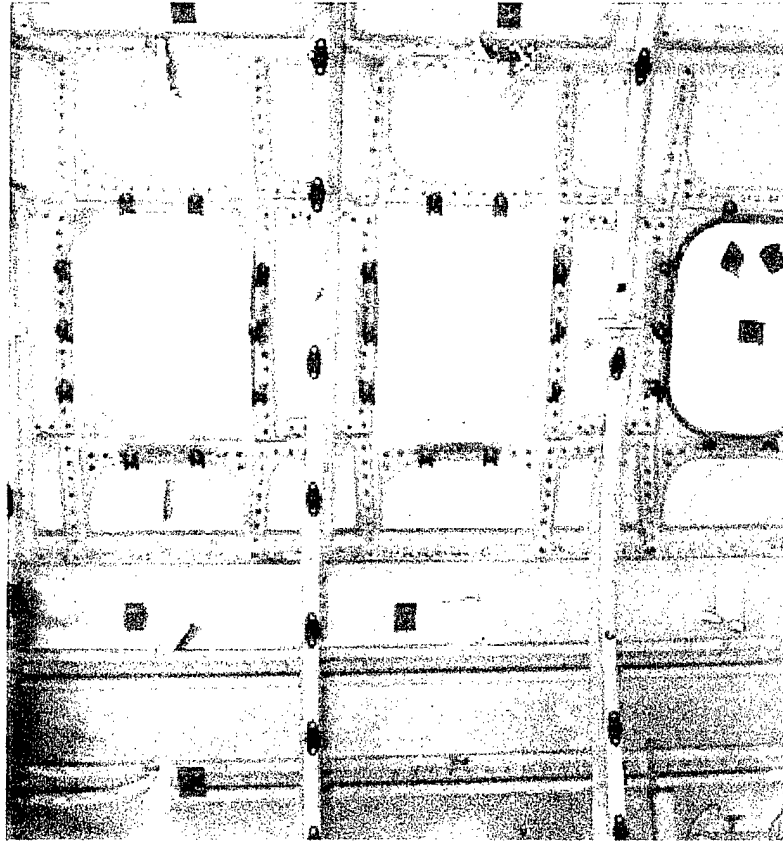FIGURE 23. EXAMPLE EXTERIOR DAMAGE AREAS

18

FIGURE 24. EXAMPLE INTERIOR DAMAGE AREAS

Figure 25 is a photograph of the blade that bounced off of the fuselage when shot at 718 ft/s and with a fragment angle of 15 deg. at impact. The 0.266-in.-thick skin was slightly dented.

FIGURE 25. A CURLED BLADE FROM SHOT 34

2.5 CONCLUSION.

The data show that the UDM penetration equations produce excellent agreement to the actual residual energies for the skin only structure. There is a reduced agreement for the complex structures. The skin and fuel tubing shots are separated to show the possibility of the UDM producing excellent agreement for complex structures. Complex structural modeling will be expanded during Phase II test analysis. Collection of more test data in Phase II will allow an expanded UDM model examination. This test has shown the UDM penetration equations to be valid for first-cut, large fragment analysis. The test also has shown that for first-order investigations, the UDM equations can provide a reasonable prediction of the residual energies. The data indicate a potential for an improved complex modeling approach utilizing the UDM equations.

2.6 FUTURE PLANS.

A follow-on test is planned. Adding to this data and evaluating other possible approaches for modeling complex structures with the UDM penetrations equations may yield a very useful first-cut engineering tool. The follow-on tests candidates will include higher obliquity angles, higher impact angles, larger blades, and thicker metal targets.

3. REFERENCES.

1.   Manchor, J. and Frankenberger, C., "Engine Debris Penetration Testing", Naval Air Warfare Center, Weapons Division, China Lake, CA, DOT/FAA/AR-99/19, May 1999.

2.   Erlich, D. C., Shockey, D. A., and Simons, J.W., "Full-Scale Tests of Lightweight Fragment Barriers on Commercial Aircraft", SRI International, Menlo Park, CA, DOT/FAA/AR-99/71, November 1999.

APPENDIX A—SUMMARY OF COMPLEX TEST SHOTS

A-1. NARRATIVE DESCRIPTION OF THE EXPERIMENTS.

A total of five shots (60 through 64) were conducted against very complex airframe structural elements. The location of these shots precluded the use of high-speed film for residual velocity measurements. Large areas would have to be cut away to allow for lighting and a field of view. These data are presented as documented impacts of engine debris as an example of the levels of damage that may occur. All control cables were tensioned to 80 psi. One external high-speed camera was set up to provide impact velocities. The lighting was insufficient and none of the film was readable. Using the previous shots data, a correction can be applied for the difference between the pressure and the high-speed film velocities.

An aluminum false floor was laid on the interior of the cabin to prevent blades from damaging the cabin area. Sometimes, it was successful. All material is aluminum unless otherwise noted.

The following shots serve as an indicator of the amount of damage that can be done by one fragment. Shots 63 and 64 show the vulnerability of the control cables that run under the cabin floor.

A-1.1 Shot 60.

The target was a control cable pulley and bracket in the aft section of the starboard main landing gear bay. The impact velocity based on pressure measurements was 438 ft/sec. Tables A-1 and A-2 summarize the shot specifications and results respectively.

TABLE A-1. SHOT 60 SPECIFICATIONS

Fragment Length (in)	5
Fragment Width (in)	3
Fragment Maximum Thickness (in)	0.218
Fragment Weight (gm)	152.3
Launch Pitch (deg)	-10
Launch Roll (deg)	0
V_{pres} (ft/s)	438
V_{cor} (ft/s)	469

TABLE A-2. SHOT 60 RESULTS

Element Impacted	Damage	Thickness (in)	Notes
Cables	Undamaged	0.130	
Pulley Bracket	Slightly bent		Pulley is operable
Fiberglass Duct	6″ tear	Approx. 0.10	Blade stopped at entry

The shot went high and struck two control cables at a very slight angle. The cables deflected the blade. The result was an undamaged pulley and the blade lodged in a fiberglass hot air duct.

The cables were scraped but no strands were cut. A small crack was found in the pulley bracket attachment to the wall.

A-1.2 Shot 61.

Shot 61 had the same target as Shot 60. This time the fragment flew true and impacted the pulleys. The pulley assembly was destroyed. Three cables were cut. The shot was taken again because the pulley was only slightly damaged in shot 60. Tables A-3 and A-4 summarize the shot specifications and results respectively.

TABLE A-3. SHOT 61 SPECIFICATIONS

Fragment Length (in)	7.5
Fragment Width (in)	3.9
Fragment Maximum Thickness (in)	0.291
Fragment Weight (gm)	310.9
Launch Pitch (deg)	0
Launch Roll (deg)	0
V_{pres} (ft/s)	711
V_{cor} (ft/s)	764

TABLE A-4. SHOT 61 RESULTS

Element Impacted	Damage	Thickness (in)	Notes
Cables	Severed	0.130	
Cables	Severed	0.130	
Cables	Severed	0.130	
Pulley Bracket	4″ slice	2 sides 0.070 each	Both pulleys broke in half, both sides of bracket sliced
Fiberglass Duct		Approx. 0.10	

A-1.3 Shot 62.

The objective of this shot was to impact the fuselage from a lower side toward the middle cabin floor area. The shot went through the starboard side of the forward baggage compartment and up into the cabin floor. Tables A-5 and A-6 summarize the shot specifications and results respectively.

TABLE A-5. SHOT 62 SPECIFICATIONS

Fragment Length (in)	8.4
Fragment Width (in)	2.9
Fragment Maximum Thickness (in)	0.291
Fragment Weight (gm)	309.1
Launch Pitch (deg)	0
Launch Roll (deg)	90
V_{pres} (ft/s)	790
V_{cor} (ft/s)	855

TABLE A-6. SHOT 62 RESULTS

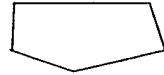| Element Impacted	Damage (in)	Thickness (in)	Notes
Outer Skin	3.5 x 0.3	0.045	6.2 in. tear up and an 11.8 in. tear down from hole. Outer skin is wing root fairing.
Hatch Panel	3.5 x 0.3	0.045	
Panel Doubler	3.5 x 0.3	0.05	
Inner Skin	3.5 x 0.3	0.075	
Hat Stringer	Severed	0.052	
Bracket	2 x 0.3	0.070	
Cable	Severed	0.130	
Cable	Severed	0.090	
Cable	Severed	0.090	
Cable	Severed	0.130	
Cable	Severed	0.130	
Strap	2.0 wide, severed	0.030	
Al & Foam Sandwich Cabin Floor	3.5 x 0.3	Al - 0.021 Foam - 0.4 Al - 0.021	
Al False Floor	3.6 x 0.1	0.125	Blade Stopped. The false floor was a test addition.

A-1.4 Shot 63.

This was the second shots into the forward baggage compartment and upward into the cabin floor. The shot was aimed at an area where a large number of cables were passing under the cabin floor. Tables A-7 and A-8 summarize the shot specifications and results respectively.

TABLE A7. SHOT 63 SPECIFICATIONS

Fragment Length (in)	7.5
Fragment Width (in)	3.0
Fragment Maximum Thickness (in)	0.281
Fragment Weight (gm)	306.3
Launch Pitch (deg)	0
Launch Roll (deg)	90
V_{pres} (ft/s)	803
V_{cor} (ft/s)	862

TABLE A-8. SHOT 63 RESULTS

Element Impacted	Damage (in)	Thickness (in)	Notes
Outer Skin	6 x 2 x 3 x 2 x 3	0.045	Polygon
Panel Doubler	0.625 x 0.5	0.05	Nicked
Skin Joint Doubler	1.5 x 0.5	0.03	
Inner Skin	3.4 x 2	0.075	
Hat Stringer	1.0 x 0.5	0.05	Nicked brim
Cable	Severed	0.090	
Cable	Severed	0.090	
Cable	Severed	0.090	
Cable	Severed	0.130	
Cable	Severed	0.130	
Floor beam web	3 x 2	0.102	
Floor beam cap	0.75 x 0.5	0.129	
Cabin Floor; Al & Balsa Sandwich	3.5 x 1	Al - 0.021 Balsa - 0.4 Al - 0.021	
False Floor		0.125	0.5 in deep dent, blade stopped

A-1.5 Shot 64.

This was the last of the shots into the cabin floor control cable area. Tables A-9 and A-10 summarize the shot specifications and results respectively.

TABLE A-9. SHOT 64 SPECIFICATIONS

Fragment Length (in)	9.437
Fragment Width (in)	3.0
Fragment Maximum Thickness (in)	0.251
Fragment Weight (gm)	333.5
Launch Pitch (deg)	0.0
Launch Roll (deg)	45
V_{pres} (ft/s)	699
V_{cor} (ft/s)	753

TABLE A-10. SHOT 64 RESULTS

Element Impacted	Damage (in)	Thickness (in)	Notes
Outer Skin	3.375 x 0.188	0.045	
Inner Skin	3.375 x 0.188	0.075	
Hat Stringer	1.75 x 0.188	0.075	¾ cut
Steel Hot Air Duct	3.75 x 0.75	0.03	Both sides
Vertical Floor Post	2.0 x 1.5	0.96	
Floor Beam Tie Strap	1.0 x 0.2	0.046	
Bracket	3.1 x 0.2	0.46	
Cable	Severed	0.13	
Al & Balsa Sandwich Floor	6.0 x 0.75	Al - 0.021 Balsa - 0.4 Al - 0.021	
False Floor	6.0 x 0.75	0.125	Blade penetrated the false floor, exited the fuselage and was lost.

A-2 ADDITIONAL DATA.

A complete photographic database of the tests exists at NAWCWD China Lake on CDROM. The files are JPEG format. There are over 700 images of the setup, each shot and results. Each shot will have three views of the fragment, an exterior view of the fuselage impact, and an interior view of the impact point. The photographs usually contain a ruler and a numbered 3.5 by 5 inch card that indicated the shot number.